

Direct Numerical Simulation of Flow and Heat Transfer From a Sphere in a Uniform Cross-Flow

P. Bagchi

Department of Theoretical & Applied Mechanics,
University of Illinois,
Urbana, IL 61801-2935

M. Y. Ha

School of Mechanical Engineering,
Pusan National University,
South Korea

S. Balachandar

Department of Theoretical & Applied Mechanics,
University of Illinois,
Urbana, IL 61801-2935

Direct numerical solution for flow and heat transfer past a sphere in a uniform flow is obtained using an accurate and efficient Fourier-Chebyshev spectral collocation method for Reynolds numbers up to 500. We investigate the flow and temperature fields over a range of Reynolds numbers, showing steady and axisymmetric flow when the Reynolds number is less than 210, steady and nonaxisymmetric flow without vortex shedding when the Reynolds number is between 210 and 270, and unsteady three-dimensional flow with vortex shedding when the Reynolds number is above 270. Results from three-dimensional simulation are compared with the corresponding axisymmetric simulations for $Re > 210$ in order to see the effect of unsteadiness and three-dimensionality on heat transfer past a sphere. The local Nusselt number distribution obtained from the 3D simulation shows big differences in the wake region compared with axisymmetric one, when there exists strong vortex shedding in the wake. But the differences in surface-average Nusselt number between axisymmetric and three-dimensional simulations are small owing to the smaller surface area associated with the base region. The shedding process is observed to be dominantly one-sided and as a result axisymmetry of the surface heat transfer is broken even after a time-average. The one-sided shedding also results in a time-averaged mean lift force on the sphere. [DOI: 10.1115/1.1358844]

Introduction

There are many examples in nature and technology where the movement of solid particles and liquid droplets play an important role (Clift et al. [1], Faeth [2], Law [3]). Understanding the particle behavior is very important in the performance prediction and enhancement of many industrial equipment. In many applications, the particulate matter is not passively advected by the surrounding fluid flow; but they actively participate in defining the surrounding flow through heat transfer, evaporation, and burning.

Even dilute systems typically consist of millions of particles that in any numerical simulation it is virtually impossible to consider the details of flow and heat transfer from each of these particles. A popular computational approach to these particulate flows has been Eulerian-Lagrangian in nature; where the continuous phase (fluid flow) is treated in an Eulerian fashion, while the distributed phase (particles) is treated Lagrangian. In applications where the particles are active, it is not sufficient to track only their position and velocity; their mass, temperature, and concentration need to be evolved in time as well. An expression for drag and lift coefficients on the particle is required to describe its motion. Additional heat transfer and mass transfer correlations are required to predict heat and mass exchange with the surrounding flow.

The force and heat transfer coefficients clearly depend on the nature of the surrounding flow, which are generally parametrized in terms of Reynolds number based on particle diameter and relative velocity, nondimensional temperature difference between the particle and the surrounding, etc. In the low Reynolds number limit analytical expression for drag coefficient dates back to Stokes. However, as Reynolds number increases flow over the sphere becomes increasingly complex, especially as Re increases above 270, the flow is three-dimensional and time-dependent with periodic vortex shedding (Natarajan and Acrivos [4], Tomboulides et al. [5]). Heat transfer around the sphere is significantly affected by this time-dependence and three-dimensionality of flow

field. At these Reynolds numbers ($Re \sim O(1)$) the only possible approach to obtaining accurate parametrization of force and heat transfer coefficients is through either careful experiments or detailed three-dimensional numerical simulations of flow around an isolated particle.

Recent explosion in computing capability has enabled detailed three-dimensional time-dependent simulation of flow past spherical particles at moderate Reynolds numbers. These simulations have allowed investigation of the resulting wake structure and drag and lift forces in both uniform and nonuniform flows (Johnson and Patel [6], Kurose and Komori [7], Mittal [8], Bagchi and Balachandar [9]). However, most effort to calculate the heat and mass transfer around drops and particles at finite Reynolds number have been limited to two-dimensional simulations, where the flow and temperature fields surrounding the sphere have been assumed to be steady and axisymmetric. Sayegu and Gauvin [10] carried out the numerical analysis for the fluid flow and heat transfer around a sphere using finite difference techniques for Reynolds numbers up to 50. Average Nusselt number correlation was obtained which compared well with the experimental data of Ranz and Marshall [11] and Whitaker [12]. This study also considered the effect of variable properties on the fluid flow and heat transfer around a sphere. Renksizbulut and Yuen [13] numerically studied droplet evaporation in a high-temperature stream for Re in the range 10–100. The effects of variable properties and mass transfer (mass efflux from the droplet surface) on the fluid flow and heat transfer around a sphere were investigated. Momentum, energy, and species continuity equations were solved in a coupled manner assuming steady axisymmetric conditions. Wong et al. [14] studied the flow and heat transfer characteristics of laminar combined convection from an isothermal sphere in the range of Reynolds number of 5–100 and Grashof number of 0–80,000. The average Nusselt number correlation for the case without natural convection was compared with Yuge's experimental correlation (Yuge [15]). In addition to heat transfer calculation from a spherical particle or droplet, Chiang et al. [16] and Xin and Megaridis [17] considered the effects of variable thermo-physical properties, transient heating, internal circulation of liquid, and droplet rotation on heat and mass transfer from a spherical droplet, under the axisym-

Contributed by the Fluids Engineering Division for publication in the JOURNAL OF FLUIDS ENGINEERING. Manuscript received by the Fluids Engineering Division January 10, 2000; revised manuscript received November 17, 2000. Associate Editor: D. R. Williams.

metric condition. Dandy and Dewyer [18] obtained three-dimensional numerical solutions for steady and linear shear flow past a fixed spherical particle over a wide range of Reynolds number of 0.1–100 and dimensionless shear rates of 0.005–0.4. They studied the effects of shear rate on the drag and lift coefficients and Nusselt number.

The assumption of steady state and axisymmetric flow for a uniform flow past a spherical particle is well justified at lower Reynolds numbers considered in the above investigations. As Reynolds number increases above 210, it has been well established that the axisymmetry of the wake is broken with a *double threaded* wake; however, the flow remains steady. At Reynolds numbers greater than 270, periodic shedding of vortices is observed; as a result the flow is time-dependent and three-dimensional. To our knowledge, there is little study on the time-dependent and three-dimensional nature of heat transfer around a sphere at Reynolds numbers greater than 270. Thus, the purpose of the present study is to investigate the effects of time-dependence and three-dimensionality on the prediction of heat transfer around a sphere. Time-dependent and three-dimensional results are compared with those based on steady and axisymmetric flow approximation.

Numerical Methodology

Here we consider the problem of flow of heat transfer from an isothermal sphere of temperature, T_s , subjected to a uniform cross-flow of relative velocity, U_∞ , and constant farfield temperature of T_∞ . The particle is assumed to be stationary (or at most moving at constant velocity without acceleration) and without any spin. We solve the continuity, Navier-Stokes and energy equations in their nondimensional form in a frame of reference fixed on the spherical particle

$$\nabla \cdot \mathbf{u} = 0$$

$$\frac{\partial \mathbf{u}}{\partial t} + \mathbf{u} \cdot \nabla \mathbf{u} = -\nabla p + \frac{1}{\text{Re}} \nabla^2 \mathbf{u} \quad (1)$$

$$\frac{\partial T}{\partial t} + \mathbf{u} \cdot \nabla T = \frac{1}{\text{Pr Re}} \nabla^2 T.$$

In the above equations, diameter of the spherical particle, d , is the length scale, the freestream velocity in the frame of reference fixed on the particle, U_∞ , is the velocity scale. The nondimensional temperature is defined as $T = (T^* - T_\infty)/(T_s - T_\infty)$, where T^* is the dimensional temperature and \mathbf{u} and p are the nondimensional velocity and pressure of the fluid flow. The above nondimensionalization results in two dimensionless parameters: $\text{Re} = dU_\infty/\nu$ and $\text{Pr} = \nu/\kappa$, where ν and κ are the kinematic viscosity and thermal diffusivity of the fluid. In the simulations to be reported here the Prandtl number, Pr , has been taken to be 0.72 corresponding to that of air.

The governing equations are solved in spherical coordinates (r, θ, ϕ) where $r_p \leq r \leq r_d$, $0 \leq \theta \leq \pi$ and $0 \leq \phi \leq 2\pi$. Here r_p represents the particle radius and r_d represents the boundary of the computational domain. θ and ϕ are the tangential and azimuthal directions, respectively. In the nonperiodic radial direction a Chebyshev collection scheme is used. In order to resolve the shear layer near the sphere surface, a radial grid stretching is used to cluster more points. The azimuthal direction is periodic over 2π and a Fourier expansion is used with a uniform distribution of collocation points in ϕ . In the θ direction, variables are defined only over π and therefore a sine or cosine expansion is used in θ as appropriate. A grid stretching is also used in θ to cluster points in the wake region of the sphere.

A two-step time-split scheme is used to advance the flow field. First, the velocity field is advanced from time level “ n ” to an intermediate level by solving the advection-diffusion equation. In the advection-diffusion step, the nonlinear terms and the θ -diffusion terms are treated explicitly using second-order

Adams-Bashforth scheme. The radial and azimuthal diffusion terms are treated implicitly using Crank-Nicholson scheme. Then a Poisson equation for pressure is solved fully implicitly. The final divergence-free velocity field at “ $n+1$ ” is obtained with a pressure-correction step. The temperature field is advanced in a similar manner with second-order Adams-Bashforth for the advection term and Crank-Nicholson scheme for the diffusion term. Once the velocity and temperature fields are obtained, force acting on the particle is computed by

$$F_i = \int_S [-p \mathbf{e}_r + \tau_{r\theta} \mathbf{e}_\theta + \tau_{r\phi} \mathbf{e}_\phi] \cdot \mathbf{e}_i dS \quad (2)$$

where the integration is over the surface of the sphere. The first term on the right corresponds to the pressure force, and the next two terms correspond to the viscous force. A nondimensional force coefficient is defined using the scaling parameters mentioned above as

$$C_F = \frac{\mathbf{F}^*}{\frac{1}{2} \rho U_\infty^2 \pi (d/2)^2}, \quad (3)$$

where \mathbf{F}^* is net force on the particle in dimensional terms. In terms of corresponding nondimensional force given in Eq. (2), the force coefficient becomes $C_F = 8\mathbf{F}/\pi$. The component of C_F along the direction of relative velocity is then the drag coefficient, C_D , and the component perpendicular to drag will be the lift coefficient, C_L . Local heat transfer from the sphere is calculated as

$$h(\theta, \phi) = \nabla T \cdot \mathbf{e}_r \quad (4)$$

From the above nondimensional form the local heat transfer coefficient is the same as local Nusselt number. Surface-averaged Nusselt number is then defined as

$$\overline{\text{Nu}} = \frac{1}{\pi} \int_S \text{Nu}(\theta, \phi) dS \quad (5)$$

where the integral is over the surface of the sphere, whose nondimensional radius is $1/2$.

A uniform flow is specified at the inlet to the computational domain. At the outflow, a nonreflecting boundary condition is used (Mittal and Balachandar [19]). Here the governing equations are smoothly parabolized by multiplying the radial diffusion terms by a filter function. On the surface of the sphere, the no-slip and no-penetration conditions are imposed.

In a spherical coordinate system, the azimuthal resolution near the poles is much higher than what is necessary to resolve the flow. The viscous stability constraint is avoided by the implicit treatment of the diffusion terms. However, a severe convective (CFL) stability constraint still exists. In order to avoid such restriction, high frequency azimuthal components are filtered out near the poles. The axisymmetric mode $k_\phi = 0$ does not lead to convective instability and need not be filtered. Also the $k_\phi = \pm 1$ modes should be retained in the entire computational domain as these modes are the source of asymmetry and unsteadiness in the sphere wake. For the higher order Fourier modes along the azimuthal (ϕ) direction, we apply a smooth filter in both r and θ . The filtering is localized to a small region near the poles and the size of the region increases with the azimuthal mode. The details of numerical methodology can be seen in (Bagchi and Balachandar [9]).

Results and Discussion

First, we shall consider the structure of the wake in the steady flow regime. Figure 1 shows the streamline, azimuthal vorticity, and dimensionless temperature distribution past a sphere for $\text{Re} = 200$. When Reynolds number is less than 210, it is known that the sphere wake in a uniform flow remains symmetric and steady, giving rise to the observed symmetric flow and dimensionless

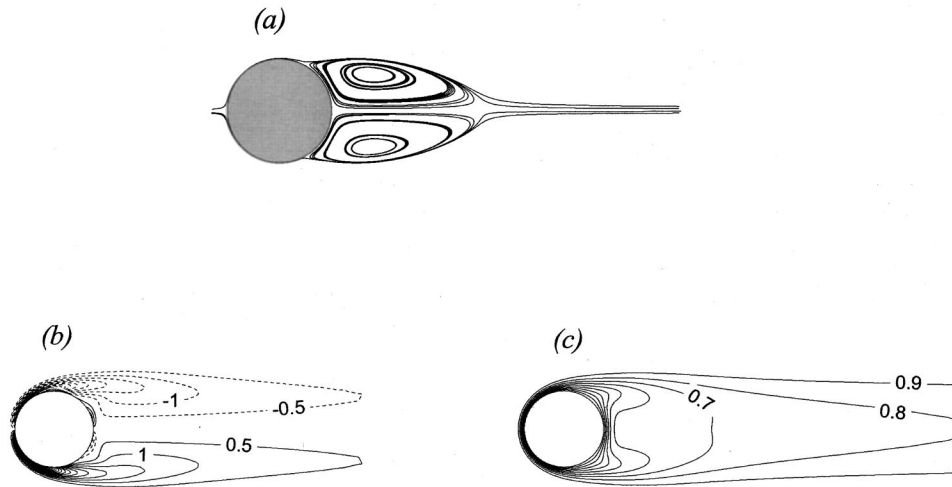


Fig. 1 Axisymmetric flow at $Re=200$. (a) Streamlines; (b) azimuthal vorticity (ω_ϕ) contours at an interval of 0.5; dashed lines indicate negative values; (c) dimensionless temperature at an interval of 0.1.

temperature fields past a sphere for $Re=200$. The gradient of dimensionless temperature is the largest at the front stagnation point ($\theta=\pi$) and decreases with increasing thermal boundary layer thickness along the streamwise direction. The maximum thermal boundary layer appears to be close to the point of flow separation. In the wake region, the flow is recirculating and the gradient of dimensionless temperature decreases again reaching a local minimum at the rear stagnation point. This behavior qualitatively remains the same over the range of Reynolds number from about 10–210, when the flow is steady and axisymmetric, and the size of the wake recirculation region progressively increases with increasing Reynolds number.

Figure 2 shows the variation of local Nusselt number over the sphere as a function of θ for different Reynolds numbers of 50, 100, and 200. In the present coordinate system $\theta=0$ corresponds to the rear stagnation point and $\theta=\pi$ corresponds to the front stagnation point and $\theta=\pi/2$ corresponds to the equatorial plane dividing the leeward ($\theta<\pi/2$) and windward ($\theta>\pi/2$) sides of the sphere. When the Reynolds number is small, at $Re=50$, the local Nusselt number has a maximum at the front stagnation point and decreases monotonically along the streamwise direction with increasing thermal boundary layer thickness, reaching a plateau in

the wake region. When Re is increased, the local Nusselt number in the wake region increases due to increasing strength of the recirculating flow. The local Nusselt number increases with increasing Re owing to increasing effect of forced convection. At $Re=200$, the local minimum in Nu can be observed to coincide with the location of flow separation and the thicker thermal boundary layer. Figure 3 shows contours of local Nusselt number on the surface of the spherical particle for $Re=200$. The view is along the negative x -axis looking upstream from the wake region. Thus the region observed is the rear half of the sphere from $\theta=0$ to $\pi/2$. Thus, Nusselt number has a larger value at $\theta=\pi/2$, decreases along the streamwise direction up to about the point of separation ($\theta\approx 0.8$) and increases again as the rear stagnation point is approached. The contours in Fig. 3 are concentric, representing that the flow and thermal fields past a sphere at $Re=200$ are axisymmetric.

When Re increases, it is known that the flow undergoes a regular bifurcation at around 210, resulting in the development of a nonaxisymmetric wake. However, the wake still remains steady

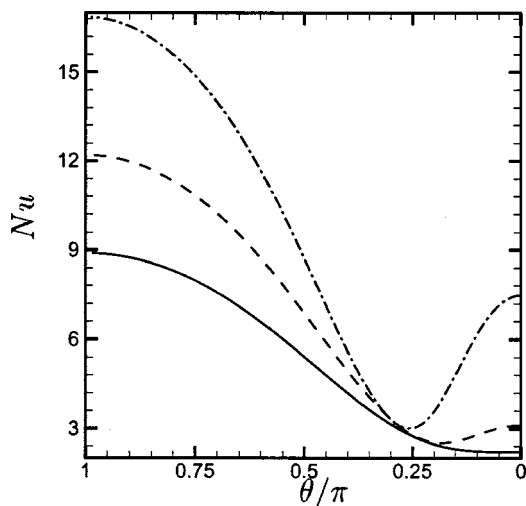


Fig. 2 Variation of Nusselt number for axisymmetric flow over the sphere: —, $Re=50$; ---, $Re=100$; - · - · -, $Re=200$.

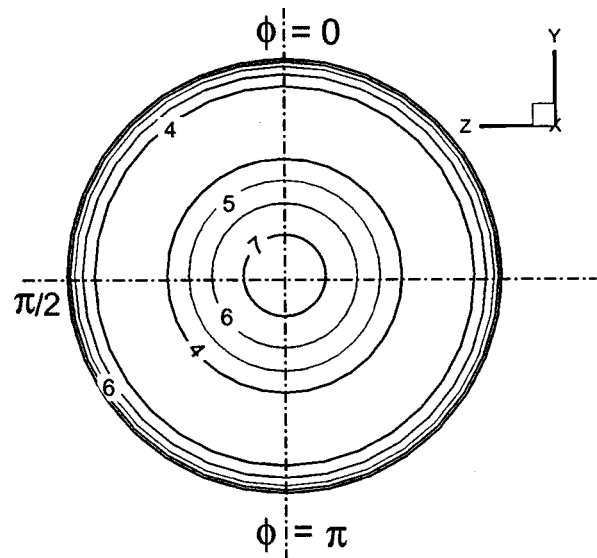


Fig. 3 Contours of Nusselt number on the sphere surface for $Re=200$.

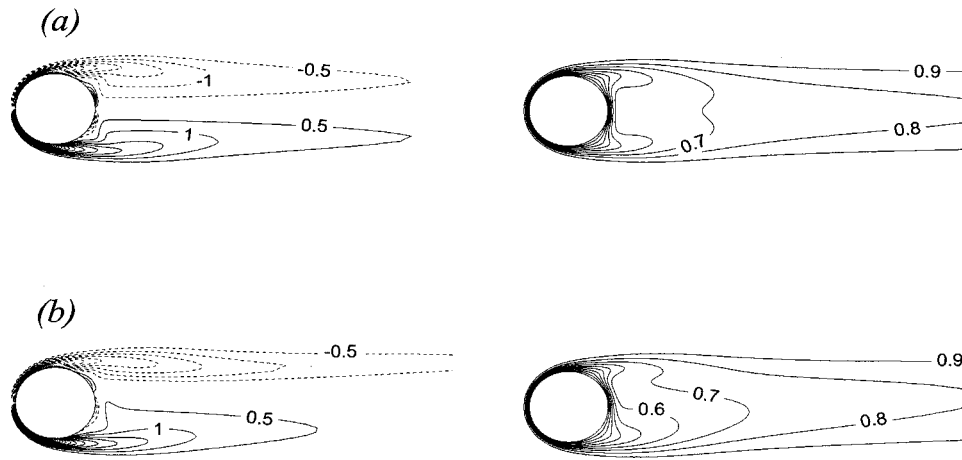


Fig. 4 Contours of azimuthal vorticity (ω_ϕ) (left panel) and dimensionless temperature (right panel) at $Re=250$. ω_ϕ contours are plotted at an interval of 0.5 while temperature contours are plotted at an interval of 0.1. Dashed lines indicate negative values. (a) Results from axisymmetric simulation; (b) results from 3-D simulation.

without vortex shedding. While the steady axisymmetric wake is *single threaded*, the steady nonaxisymmetric wake is *double threaded* (Nataragan and Acrivos [4] and Wu and Faeth [20]). Figure 4 shows contours of azimuthal vorticity and dimensionless temperature at $Re=250$. Figures 4(a) and (b) represent the results obtained from two different simulations, in order to compare them; (a) from an axisymmetric simulation where the flow is forced to be axisymmetric and (b) from a three-dimensional simulation. When axisymmetry is broken, there exists a plane passing through the streamwise (x)-axis about which the flow is symmetric (Mittal [8]). The exact orientation of this plane of symmetry is arbitrary and in the present three-dimensional simulation without loss of generality the x - y plane is chosen to be the plane of symmetry. The nonaxisymmetric nature of the wake is most clear on this plane of symmetry. The azimuthal vorticity and dimensionless temperature obtained from the three-dimensional calculation plotted on the plane of symmetry display nonsymmetric nature of the wake and are different from those obtained from the axisymmetric simulation. For example, in Fig. 4(b) the rear stagnation

point can be seen to shift upwards to $\theta \approx 18^\circ$, with corresponding asymmetric thinning of the thermal boundary layer. However, the impact of three-dimensionality in azimuthal vorticity and dimensionless temperature is not large.

Figure 5 shows variation of Nusselt number as a function of θ for $Re=250$. Here the 3D local Nusselt number (Nu) are shown at three different ϕ locations of 0, $\pi/2$, and π . The ϕ -averaged Nusselt number, defined as $\langle Nu \rangle = 1/2\pi \int_0^{2\pi} Nu d\phi$, is represented by the thick solid line and is compared with that obtained from the axisymmetric simulation. The effect of nonaxisymmetry can be seen only in the wake in terms of the large variation in the Nusselt number for the three different ϕ values, especially for $\theta < 0.3\pi$. Contours of local Nusselt number on the sphere surface for $Re=250$ obtained from the axisymmetric and 3D simulations are shown in Figs. 6(a) and (b) (again the view is from the wake and only the rear half of the sphere is shown). In the front half of the sphere the thermal field is nearly axisymmetric. The effect of three-dimensionality can be seen in Fig. 6 as the upward shift in the rear stagnation point with increased heat transfer above and decreased heat transfer below the x - z plane.

Above $Re \approx 270$ the solution undergoes Hopf bifurcation resulting in a periodic shedding of vortices in the wake. Figure 7 shows contours of azimuthal vorticity and dimensionless temperature for $Re=350$. Figure 7(a) shows the result of axisymmetric simulation and Figs. 7(b)–(e) show results of the corresponding 3D simulation at four different time instants. At this Re the flow is not

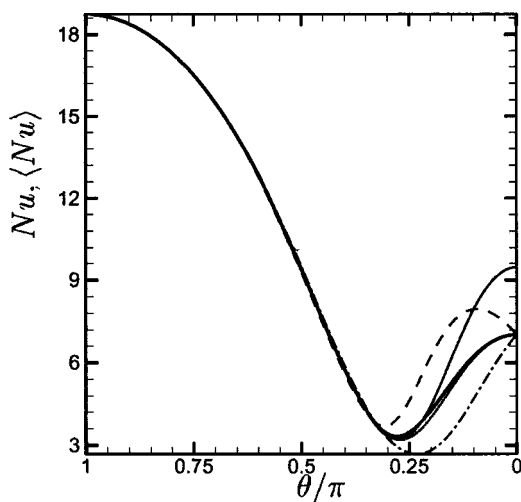


Fig. 5 Variation of Nusselt number for $Re=250$. —, Nu obtained from axisymmetric simulation. Nu obtained from 3-D simulations are shown at three different ϕ locations: ---, $\phi=0$; - · - · -, $\phi=\pi/2$; · · · ·, $\phi=\pi$. The thick line represents ϕ -averaged Nusselt number ($\langle Nu \rangle$) obtained from 3-D simulation.

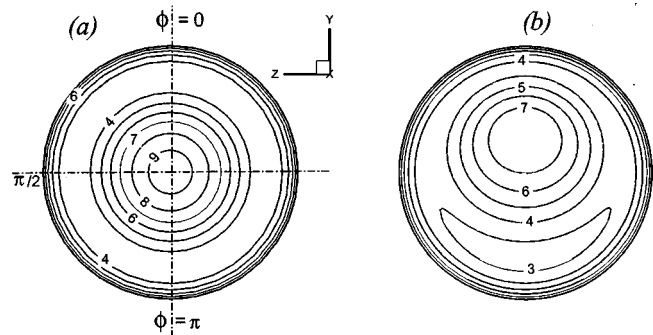


Fig. 6 Contours of local Nusselt number on the surface of the sphere for $Re=250$. (a) Results from axisymmetric simulation; (b) results from 3-D simulation.

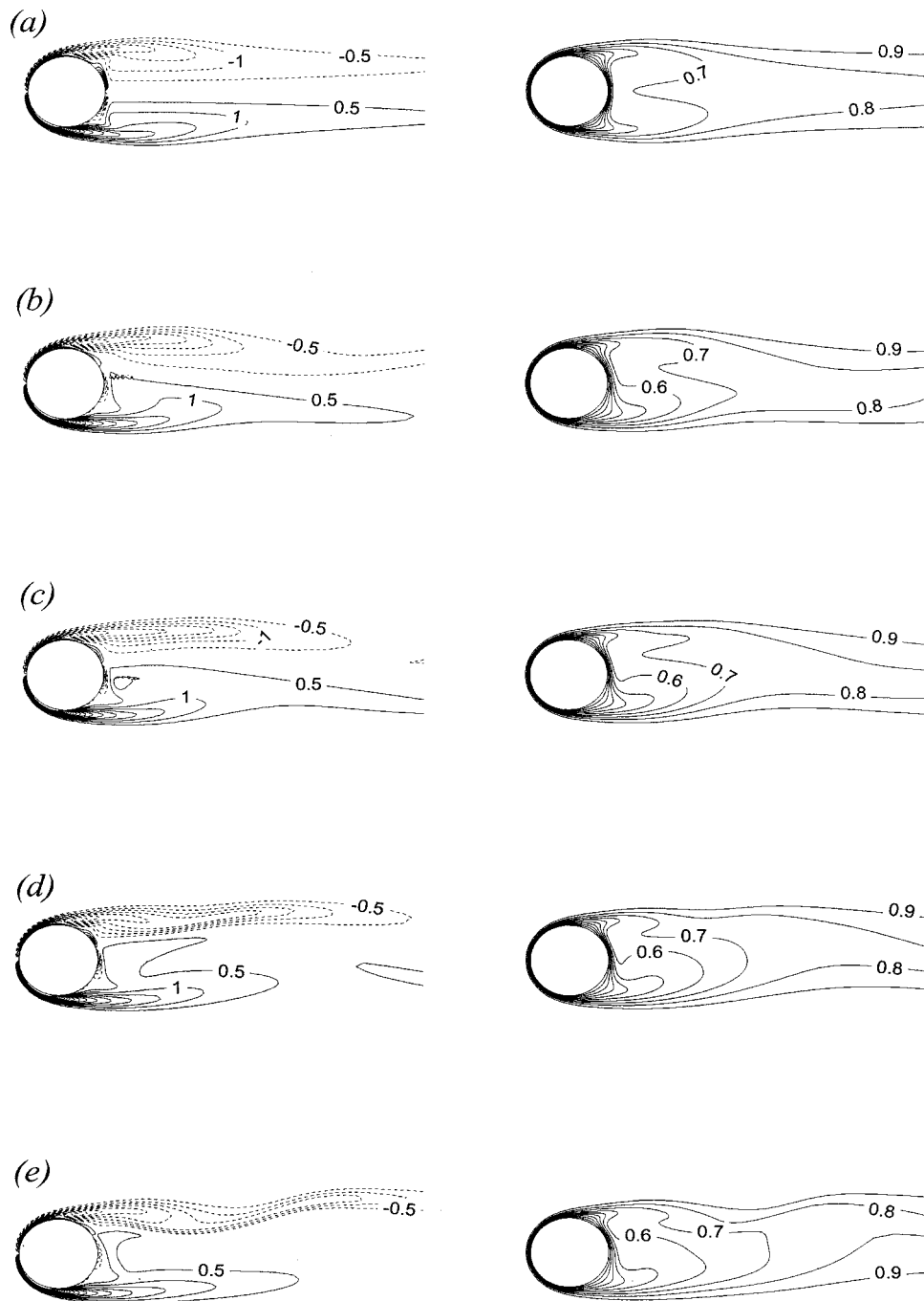


Fig. 7 Contours of azimuthal vorticity (ω_ϕ) (left panel) and dimensionless temperature (right panel) at $Re=350$. ω_ϕ contours are plotted at an interval of 0.5 while temperature contours are plotted at an interval of 0.1. Dashed lines indicate negative values. (a) Results from axisymmetric simulation. Results of 3-D simulation are presented in (b), (c), (d), and (e) at four different time instants approximately at equal interval in a shedding cycle.

precisely periodic (see Fig. 11); nevertheless, an approximate period of shedding T_p can be established. Figures 7(b)–(e) are (1/3)rd shedding period apart. At $Re=350$ the vortex shedding process is one-sided (Mittal [8]); in the present simulation vortices are shed only from the top of the sphere and not from the bottom. In this respect vortex shedding from a sphere is distinctly different from that of a circular cylinder. The one-sided shedding has its roots in the existence of the steady nonaxisymmetric wake prior to the on-set of shedding. The manifestation of the one-sided shedding process can be seen in Fig. 7, where the asymmetric contours are not seen to clearly oscillate up and down the wake centerline

as they would in the case of flow over a circular cylinder. For example, the thinning of the thermal boundary layer near the rear stagnation point remains above the centerline over the entire shedding cycle, although oscillatory behavior can be observed.

Figure 8 shows variation of Nusselt number for $Re=350$ as a function of θ at the four different time instants shown in Fig. 7. The local Nusselt numbers at three different ϕ locations of 0, $\pi/2$, and π obtained from the 3D simulation are compared with the ϕ -averaged Nusselt number represented by the thick solid line and the axisymmetric Nusselt number. Contours of local Nusselt number on the sphere surface obtained from the axisymmetric and 3D

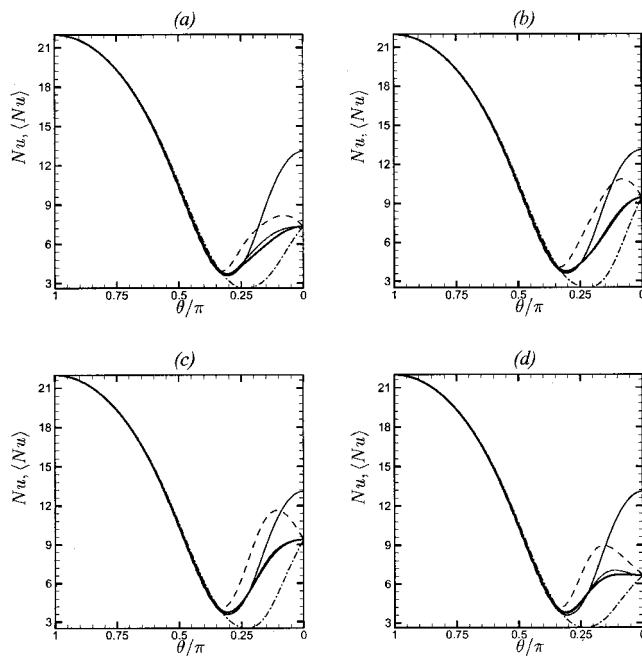


Fig. 8 Variation of Nusselt number for $Re=350$. (a), (b), (c), and (d) represent four different time instants in the shedding cycle corresponding to Fig. 7. —, Nu obtained from axisymmetric simulation. Local Nu obtained from 3-D simulations are shown at three different ϕ locations: ---, $\phi=0$; - · - · -, $\phi=\pi$; · · · ·, $\phi=\pi/2$. The thick line represents ϕ -averaged Nusselt number $\langle Nu \rangle$ obtained from 3-D simulation.

simulations for $Re=350$ are shown in Fig. 9. Similar to the case of $Re=250$, the local Nusselt number distribution on the windward side of the sphere is not influenced much by the nonaxisymmetric nature of the wake. However, in the wake region, the local Nusselt number obtained from the three-dimensional simulation shows large variation for different azimuthal (ϕ) locations and time instances. Local variation in ϕ can be in excess of 100%; for example, in Fig. 8(d) at $\theta \approx 0.25\pi$, Nu varies from 3–9. When results for $Re=350$ are compared with those for $Re=250$, the extent of three-dimensionality in local Nusselt number can be seen to

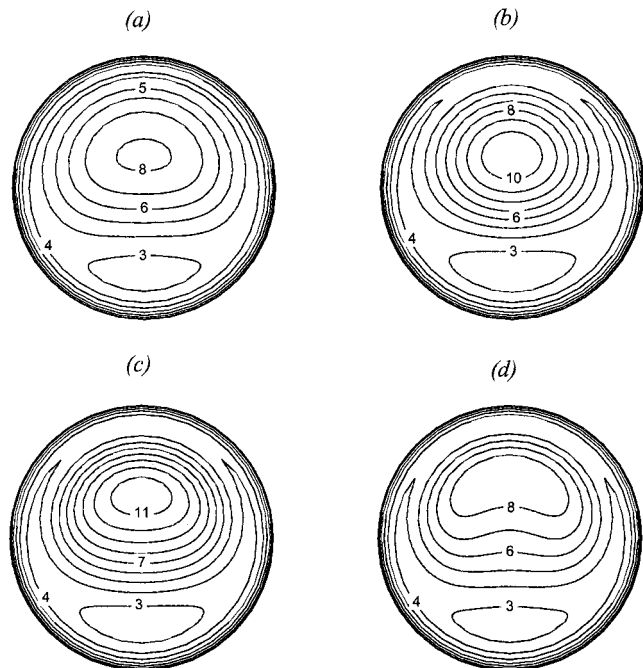


Fig. 9 Contours of Nusselt number on the surface of the sphere for $Re=350$ from the 3D simulations. Four different time instants are shown and they are the same as in Figs. 7 and 8.

increase with increasing Re . Significant difference exists between the axisymmetric result and the ϕ -averaged three-dimensional Nu distribution. The maximum difference is at the geometric pole on the leeward side ($\theta=0$). The axisymmetric approximation tends to overpredict the local heat transfer and the level of overprediction increases with Reynolds number. For example, at $Re=250$ the actual local Nu at $\theta=0$ is 7.03 while the corresponding axisymmetric approximation estimates local Nu to be 9.48—a 35% overprediction. At $Re=350$ the actual local Nu (averaged over time) predicted by the three-dimensional simulation is 8.2, while the estimate of the corresponding axisymmetric approximation is 13.1—a 60% overprediction.

Figure 9 shows significant deviation in the Nu contours away

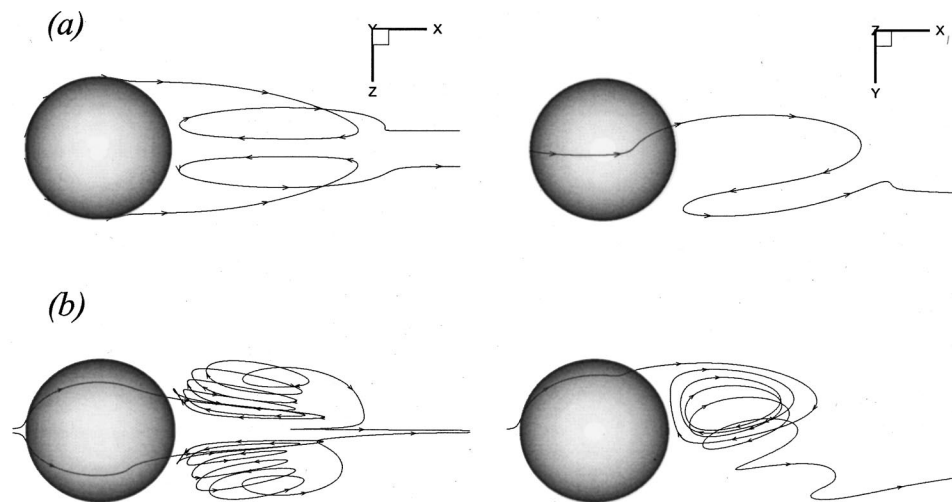


Fig. 10 Instantaneous pathlines for Reynolds number (a) 250 and (b) 350. Figures in the left panel show the pathlines that originate on two sides of the x - y plane. In the right panel, the x - y view, two particle paths coincide.

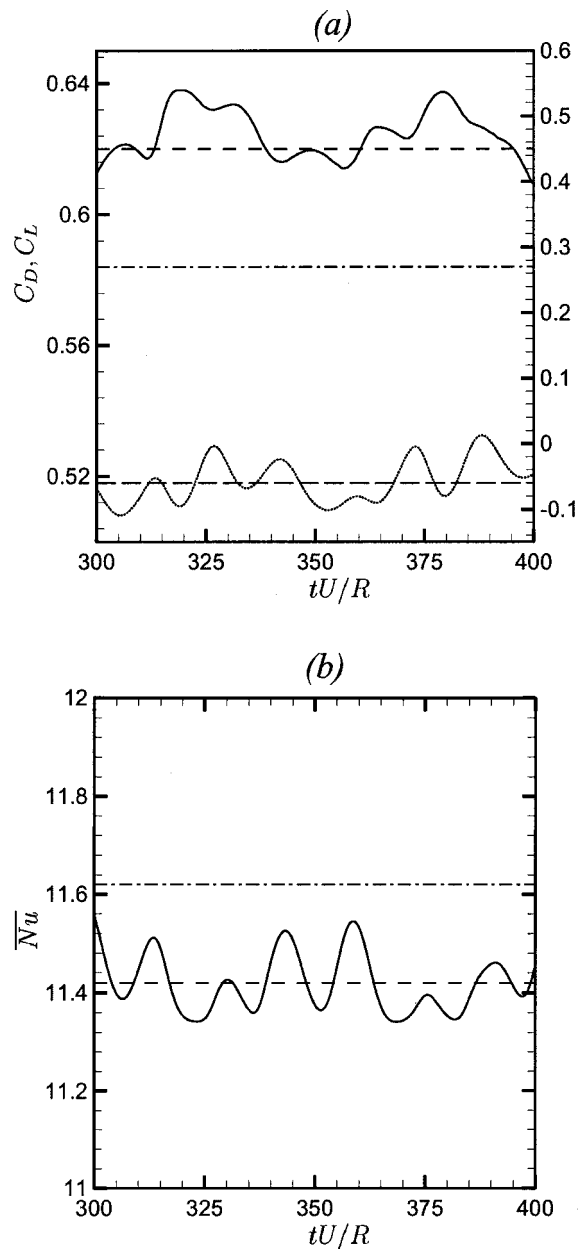


Fig. 11 Time evolution of drag and lift coefficients and surface-averaged Nusselt number \overline{Nu} for $Re=350$. (a) Vertical axis on the left is for C_D and that on the right is for C_L . —, C_D obtained from 3-D simulation; ---, mean (time-averaged) drag coefficient; ····, C_D obtained from axisymmetric simulation; ····, C_L obtained from 3-D simulation; ---, mean (time-averaged) lift coefficient. (b) —, \overline{Nu} obtained from 3-D simulation; ---, mean (time-averaged) \overline{Nu} ; ····, \overline{Nu} obtained from axisymmetric simulation.

from axisymmetry. Over the entire cycle the local Nusselt number maxima corresponding to the rear stagnation point is located on the upper side of the sphere, consistent with the observations of Fig. 7. The location of the local Nu peak seems to oscillate between 12 to about 40 deg, which can also be seen in Fig. 8 in the movement of the peak in the Nu distribution for $\phi=0$.

In the 3D simulation the nonaxisymmetric and time-dependent nature of the flow contributes to enhanced mixing in the wake. This can be seen in Fig. 10, where two sample instantaneous pathlines in the wake of the sphere are plotted for $Re=250$ and 350 . The left panel shows the trajectory projected on the $x-z$ plane

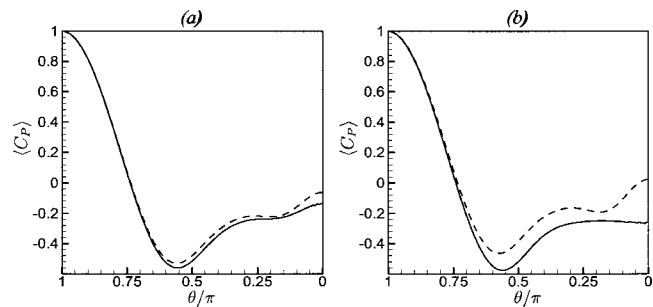


Fig. 12 ϕ -averaged surface pressure coefficient $\langle C_p \rangle$ for (a) $Re=350$ and (b) $Re=500$. Dashed line is the result from axisymmetric simulations and solid line is the result from 3-D simulations.

and the right panel shows the projection on the $x-y$ plane. The starting position of the two pathlines are symmetrically placed on either side of the $x-y$ plane, thus the two pathlines coincide on the right panels. At $Re=200$, when the flow is steady and axisymmetric, the wake bubble is closed and the streamlines are the same as pathlines. From Fig. 1(a) it can be seen that pathlines that originate upstream of the cylinder go around the closed bubble, suggesting that there is no mixing in the wake. At $Re=250$, axisymmetry is broken and results in certain amount of mixing between the wake fluid and the oncoming freestream fluid. At even higher Reynolds number ($Re=350$) the wake is unsteady and as a result of the vortex shedding process a wake bubble exists only in the mean; significant mixing between the wake and the freestream fluid can be observed. Based on this enhanced mixing one might expect higher heat transfer in the wake when the assumption of axisymmetry is relaxed. On the other hand, in the case of axisymmetric flow, a focused recirculation region exists and one can expect a strong stagnation point flow directed toward the wake region in this case. From Fig. 8 it is clear that at $Re=350$, the strength and the influence of the recirculation eddy far outweighs any potential benefits of enhanced mixing due to three-dimensionality, as far as heat transfer is concerned.

Figure 11 shows time evolution of drag and lift coefficients and surface-averaged Nusselt number (Nu) for $Re=350$. The results obtained from the 3D simulation are compared with those obtained from the axisymmetric simulation. Also shown are the time averaged results for the 3D simulation (the axisymmetric results are steady state). The signature of vortex shedding is evident in the time-dependent oscillatory nature of C_D , C_L , and \overline{Nu} . As indicated earlier, the shedding process appears to be irregular at $Re=350$ and therefore a perfect periodic variation is not observed. The approximate shedding period, based on average time between adjacent peaks in the lift coefficient is $T_p = 14.8$, corresponding to a nondimensional Strouhal number ($St = d/U_\infty T_p$) of 0.135. As expected the oscillation in drag coefficient is at about twice the shedding frequency. The time averaged drag coefficient obtained from the 3D simulation is 0.62 and the corresponding axisymmetric approximation underpredicts drag coefficient by about 5% with a C_D of 0.58. This underprediction of drag when three-dimensionality is ignored is contrary to the case of two-dimensional cylinders, where drag is overpredicted when the effect of three-dimensionality in the wake is ignored (Mittal and Balachandrar [21]).

The difference in behavior is significant and can be explained as follows. In the case of a cylinder, vortex shedding is possible even when restricted to 2D simulation and in fact the shed vortices are stronger and remain more coherent in the absence of three-dimensionality. As a result, the Reynolds stress distribution in the wake is higher in 2D simulation. The enhanced Reynolds stress leads to higher suction pressure and overprediction of drag. In the case of a sphere, the assumption of axisymmetry precludes vortex

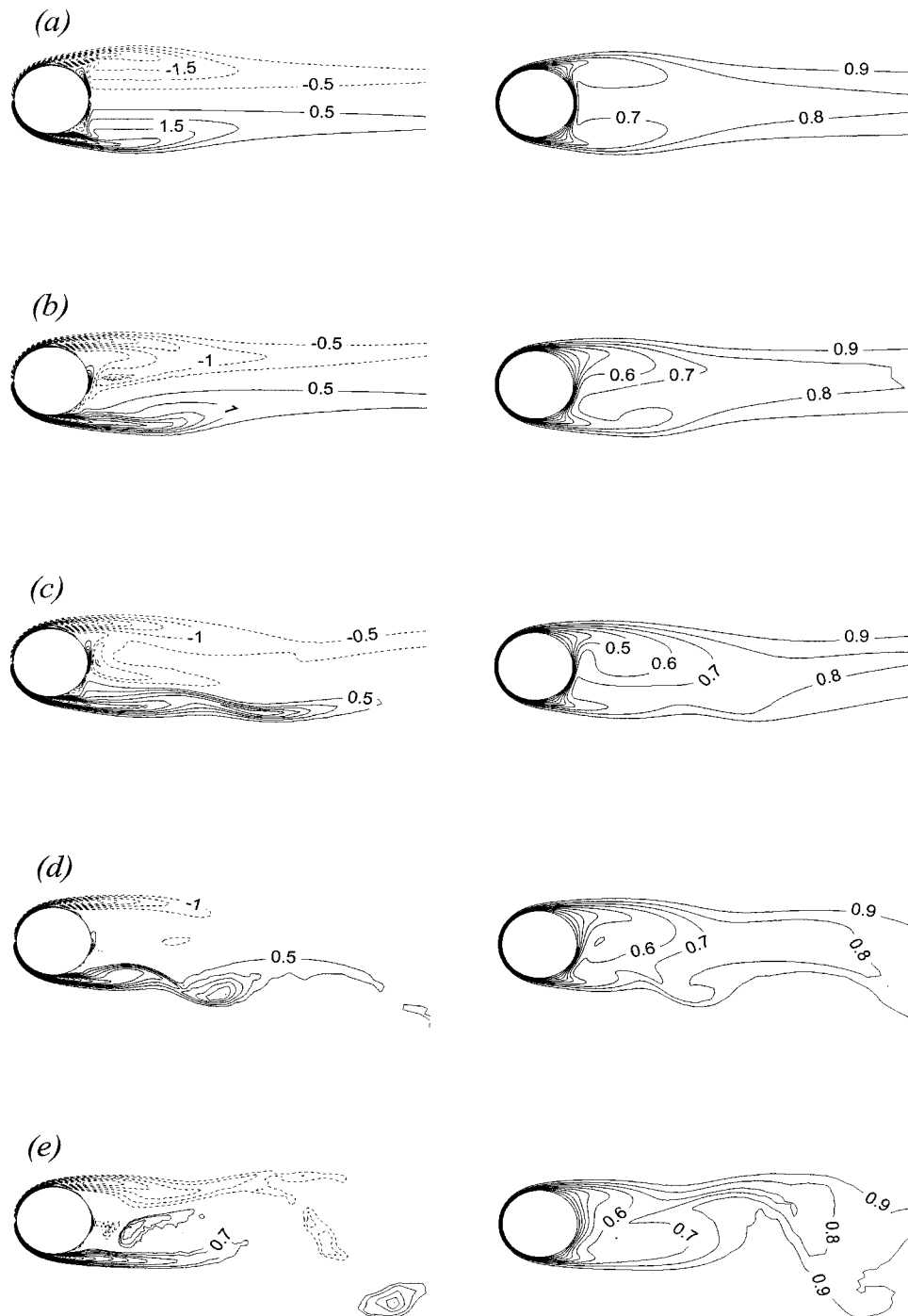


Fig. 13 Same as Fig. 7 but for $Re=500$. Time instants for the unsteady simulations (b, c, d and e) are at approximately equal interval in a shedding cycle.

shedding and time dependence; thus Reynolds stress is zero. The pressure distribution around the surface of the sphere with and without the assumption of axisymmetry is shown in Fig. 12. In the case of three-dimensional simulations ϕ -averaged surface pressure is plotted. Pressure distribution over the windward side is not significantly influenced by differences in the wake structure; however, substantial differences exist in the wake region and, in particular, the effect of three-dimensionality is to decrease the base pressure, thus explaining the higher drag.

Furthermore, unlike the case of a circular cylinder, for the sphere the time-averaged lift is nonzero. The mean C_L is observed to be -0.06 and is consistent with the one-sided shedding of the

wake vortices. The plane of symmetry that was observed at $Re=250$ persists even at $Re=350$, which can be seen in the x - z projection of pathline in Fig. 10.

Figure 13 shows contours of azimuthal vorticity and dimensionless temperature at a even higher Reynolds number of $Re=500$, obtained with an axisymmetric assumption (Fig. 13(a)) and from the three-dimensional time-dependent simulation (Figs. 13(b)–(e)). In the case of time-dependent simulation four different time instants are shown, which are separated by approximately $(1/3)$ rd shedding period. At this Re , the wake oscillation can be seen to have increased with a more chaotic shedding pattern with larger and stronger vortices than that for $Re=350$. As a result, deviation

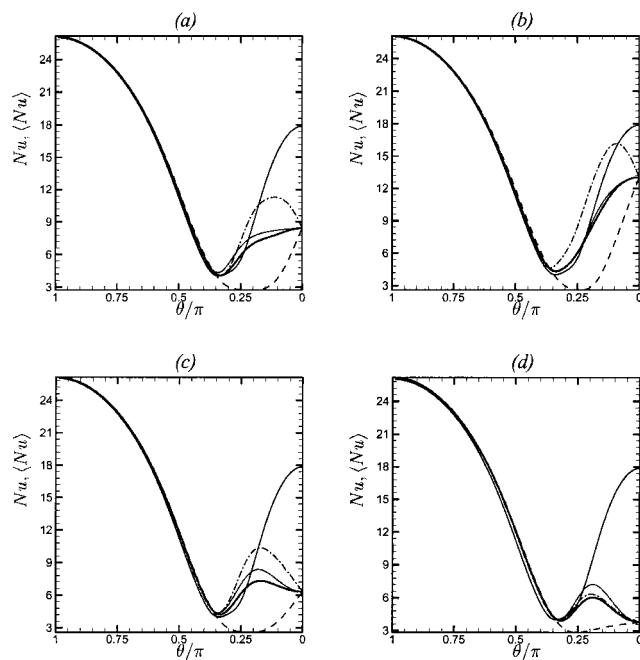


Fig. 14 Variation of Nusselt number for $Re=500$ at four different time instants: *a*, *b*, *c* and *d* represent same time instants as in Fig. 13 corresponding to the unsteady simulation. Symbols used here are same as in Fig. 8.

in both azimuthal vorticity and temperature fields from the axisymmetric case is enhanced. Figure 14 shows the θ -variation in local and ϕ -averaged Nusselt number at the four different time instances shown in Fig. 13 obtained from the 3D simulation. Also shown for comparison are the local Nusselt number obtained from the axisymmetric simulation. The impact of strong vortex shedding at this Reynolds number can be seen in the large temporal-variation in the Nusselt number in the wake region. For example, the local Nu at $\theta=0$ can be seen to vary between 3.6–13.0 over a shedding cycle. As a result the axisymmetric prediction can grossly overestimate local heat transfer in the wake region over most of the shedding cycle. The time-averaged local Nu at $\theta=0$ is about 7.9, while the corresponding prediction by the axisymmetric simulation is about 18, resulting in an overprediction of 130%. Of course, the overprediction in terms of instantaneous local heat transfer can be even higher.

The location and the motion of the separation and the rear stagnation points can be further investigated in the contours of local Nusselt number on the sphere surface shown in Fig. 15. The 3D results are shown corresponding to the four time instances shown in Fig. 13. Due to the strong vortex shedding in the wake region, contours of local Nusselt numbers on the sphere surface in the wake have a nonconcentric shape. Strong time-dependence is also observed. When compared to Fig. 9 the extent of deviation from axisymmetry is observed to increase with increasing Reynolds number. Especially in Fig. 15(*d*) the contours can be observed to symmetrically split into two with local peaks located on either side of the x - y plane, whereas the local minima still remains on the x - y plane. As a result, at this time a local peak is observed in the ϕ -averaged Nusselt number as well at about $\phi=45$ deg.

Figure 16 shows time evolution of drag and lift coefficients and surface-averaged Nusselt number for $Re=500$. At this Reynolds number the shedding process appears to be more chaotic than at $Re=350$ and the approximate nondimensional shedding frequency increases to 0.175. The time averaged drag coefficient obtained from the 3D simulation is 0.555 and the corresponding axisymmetric approximation underpredicts drag coefficient by about 10%

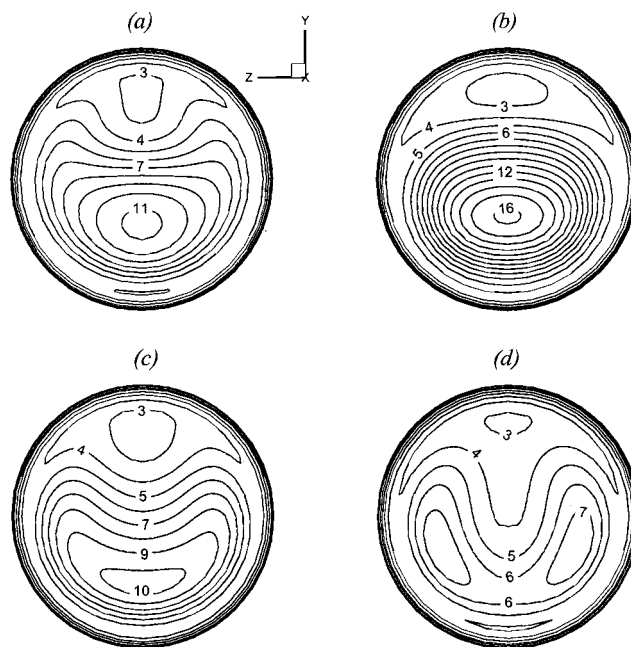


Fig. 15 Same as Fig. 9 but for $Re=500$. Results from 3D simulations are shown at four different time instants that are same as in Fig. 14.

with a C_D of 0.487. Thus the importance of three-dimensionality in accurately predicting drag increases with Re . The mean C_L is observed to be -0.048 .

At $Re=500$ the plane of symmetry that was observed at lower Reynolds numbers is somewhat broken. The chaotic shedding process is now seen to slightly oscillate—vortices are now shed over a range of azimuthal angles. Yet the transition from one-sided to all-around shedding is not complete at this Re . As a result, there is a mean negative lift. However, compared to $Re=350$ the mean negative lift is smaller in magnitude, in spite of the stronger shedding process. It can be conjectured that at even higher Re , when the near wake behavior is turbulent, vortex shedding may precess over the entire range of azimuthal angles. Correspondingly, the direction of lift force may drift in direction over time, thus resulting in a zero net lift force over long time average. However, in the present simulations up to $Re=500$, we observe the lift force to be persistent in direction over more than 15 shedding cycles. The mean lift coefficients presented here are obtained through long time average over several shedding cycles—18 shedding cycles in case of $Re=350$ and 15 shedding cycles in case of $Re=500$.

From Fig. 12 substantial influence of three-dimensionality on pressure distribution in the wake region can be observed. Although surface pressure distributions for $Re=350$ and $Re=500$ cases are qualitatively the same, increasing importance of three-dimensionality on C_D with increasing Re is clear. Mean drag is evaluated by integrating the surface pressure around the sphere with a weighting factor of $\sin(2\theta)$ (see Eq. (2)). Thus large difference in base pressure at $\theta=0$ makes little contribution to drag coefficient. The underprediction of drag coefficient is mainly due to differences in surface pressure distribution in the wake around $\theta=\pi/4$.

In Figs. 11 and 16 the time-averaged Nu in the case of 3D simulations is observed to be 11.42 and 13.27 at $Re=350$ and 500, respectively. With the assumption of axisymmetry the overall heat transfer is overpredicted by about 2% in both cases with $\bar{Nu}=11.62$ and 13.54. Thus the impact of three-dimensionality on overall heat transfer seems to be minimal and independent of Reynolds number. However, the effect of three-dimensionality cannot

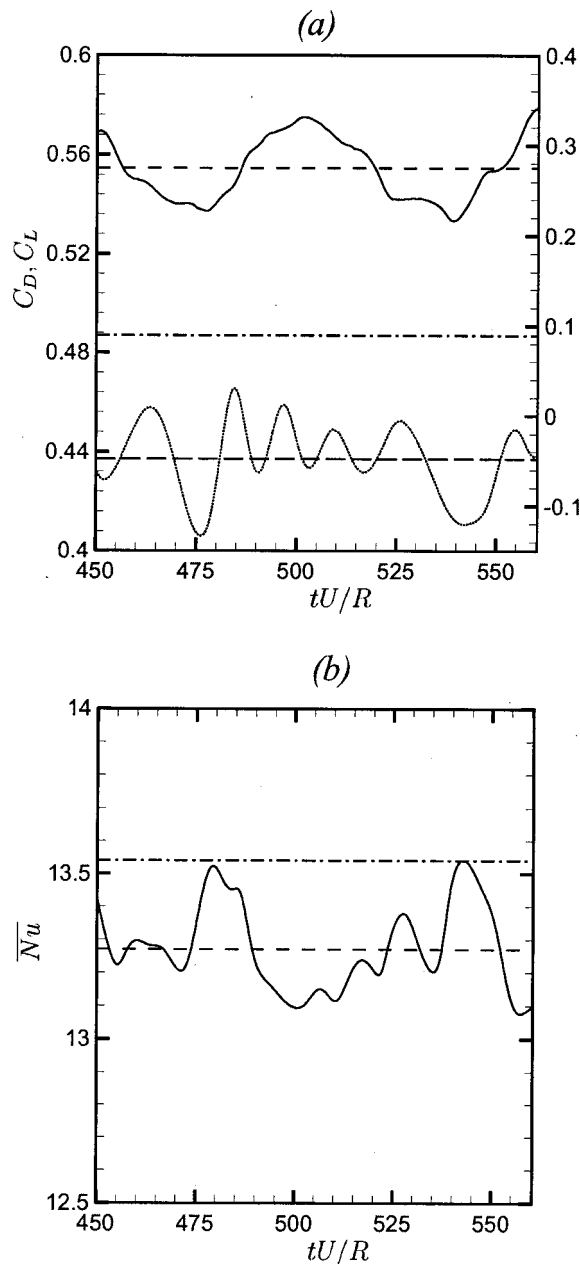


Fig. 16 Same as Fig. 11 but for $Re=500$

be ignored when it comes to local heat transfer behavior. Three-dimensionality has a strong influence on local heat transfer. As indicated in Figs. 8 and 14, local Nu near the base of the sphere can be overpredicted by several hundred percent if the flow is constrained to be axisymmetric. The difference in the local and surface-averaged behavior can be seen from the definition of \bar{Nu} (Eq. (5)), where local Nusselt number is integrated with the geometric weighting factor of $\sin(\theta)$. Most contribution to \bar{Nu} is from the equatorial region, with very little contribution from region near the poles. Thus the impact of vortex shedding on local heat transfer is much stronger than on overall heat transfer. Accurate computation of local heat transfer is important in the prediction of processes, such as evaporation, surface reaction, and surface tension, which are nonlinearly (often exponentially) dependent on temperature.

Figures 17 and 18 summarize the results of the three-dimensional simulations. C_D , C_L , and Nu obtained from the

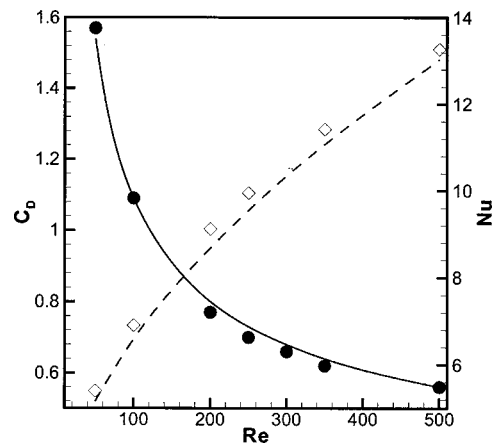


Fig. 17 Comparison of computational C_D and Nu with experimental correlations. Symbols are computational results ranging from $Re=50$ – 500 . Correlation for drag is from Clift et al. [1] and the Nu correlation is from Ranz and Marshall [11].

simulations over the Reynolds number range of 50–500 are compared with popular correlations for drag and heat transfer from a sphere given as

$$C_D = \frac{24}{Re} (1 + 0.15 Re^{0.687}) \quad \text{Clift et al. [1]}$$

$$\bar{Nu} = 2 + (0.4 Re^{1/2} + 0.06 Re^{2/3}) Pr^{0.4} \quad \text{Whitaker [12]}$$

$$\bar{Nu} = 2 + 0.6 Re^{1/2} Pr^{1/3} \quad \text{Ranz and Marshall [11]}$$

The lift coefficient is zero for $Re < 210$, as the flow is axisymmetric. Above $Re=210$ the lift coefficient is non-zero reaching a peak value of about -0.07 at $Re=300$. At higher Reynolds numbers the mean lift coefficient somewhat decreases, but remains non-zero, at least up to $Re=500$. At very large Reynolds number long time-averaged lift coefficient can be expected to approach zero owing to the turbulent nature of the wake; however, over shorter periods persistent lift force is possible. Also included in Fig. 18 are mean lift coefficient data from Johnson and Patel [6] for $210 < Re < 300$. Good agreement with the present data can be observed. The correlations shown above are based on several experimental measurements over a range of Reynolds number and therefore comparison with individual experimental measurement

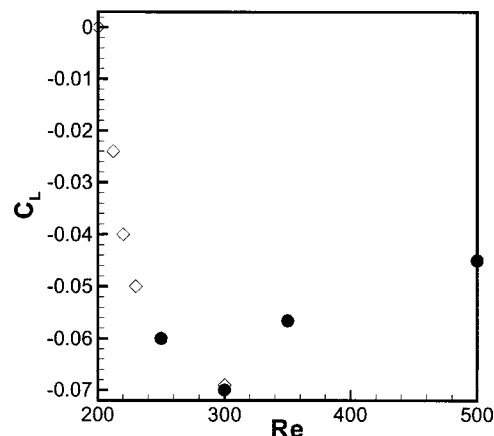


Fig. 18 The mean (time-averaged) lift coefficient versus Reynolds number for flow past a sphere. ● symbols are the results from present simulations. ◇ symbols correspond to simulation results of Johnson and Patel [6].

Table 1 Comparison of present simulations with previous experimental and numerical results

Re	Present simulations					Previous results				
	C_D	θ_s	L_e/D	St	Nu	C_D	θ_s	L_e/D	St	Nu^{\ddagger}
50	1.57	40.8	0.41		5.4	1.57*	40.0 [‡]	0.44 [*]		5.16, 5.77
100	1.09	53.2	0.87		6.91	1.09*	53.6 [‡]	0.87*		6.59, 7.32
200	0.77	63.7	1.43		9.12	0.78*	65.0 [‡]	1.29 [‡]		8.68, 9.53
250	0.70				9.95	0.70*				9.55, 10.42
350	0.62			0.135	11.42	0.62*			0.13–0.14 [¶]	11.07, 11.97
500	0.56			0.175	13.27	0.55*			0.17–0.18 [¶]	13.03, 13.91

*Clift et al. [1];

[‡]Magnaudet et al. [23];^{*}Sakamoto & Haniu [22];[‡]First Nu is obtained from Ranz and Marshal [11]; and the second value is from Whitaker [12]. For $Re \geq 250$, mean properties are listed.

is not attempted. Good agreement between these correlations and the simulation results is observed over the entire range of Reynolds numbers considered. For further validation of the present simulation; Table 1 shows a comparison of present results for separation angle (θ_s), dimensionless wake length (L_e), Strouhal number (St) for different Reynolds numbers with previous experimental and numerical results. The results for $Re \geq 210$ are surface-averaged mean values. The present results for θ_s and L_e show excellent agreement with the experimental and numerical ones over the Reynolds number ranges listed in Table 1. The Strouhal numbers for $Re=350$ and 500 are also in good agreement with experimental results given by Sakamoto and Haniu [22].

Summary and Conclusions

The heat transfer past a sphere in a uniform flow is investigated using direct numerical simulation. The solution is obtained using a highly accurate Fourier-Chebyshev pseudospectral method. When the Reynolds number is less than 210, the flow and temperature fields are axisymmetric. When Reynolds number increases above 210 (at $Re=250$), the flow and temperature fields become non-axisymmetric but without vortex shedding. But the deviation of 3D results from the axisymmetric ones is small and C_D and Nu from the 3D simulation are almost the same as those from axisymmetric one. When Reynolds number exceeds 270 ($Re=350$ and 500), the flow and temperature fields become highly three-dimensional with strong vortex shedding. Local Nusselt number distribution on the surface of the sphere significantly deviates from concentric distribution; strong variation in local Nu over time is observed, especially in the wake region.

Vortex shedding and three-dimensionality of the wake has a stronger influence on the mean drag force. Their influence on mean drag increases with Reynolds number; this behavior for the wake of a sphere is consistent with the importance of three-dimensionality in the wake of a circular cylinder. For the sphere, axisymmetric approximation results in underprediction of drag coefficient; this is in contrast to the circular cylinder where two-dimensional approximation results in overprediction of drag. In the case of a sphere, the assumption of flow axisymmetry precludes any vortex shedding (at least up to $Re=500$) and as a result temporal oscillations in lift and drag forces and surface averaged Nusselt number are features of only the 3D simulation. Vortex shedding off a sphere is predominantly one-sided, which results in a small but finite time-averaged lift coefficient.

Three-dimensionality has its strongest effect on the local heat transfer in the wake region. Heat transfer near the base of the sphere ($\theta \approx 0$) will be overpredicted by several hundred percent if three-dimensionality of the wake is ignored. This is due to the highly enhanced stagnation point flow resulting from the strong coherent recirculation bubble predicted in the case of axisymmetric assumption. In spite of this strong local effect, the impact on surface averaged Nu is not significant, owing to the smaller area associated with the base region. Thus, if the interest is only in

surface-averaged heat transfer then a simple axisymmetric simulation itself is sufficient. However, the instantaneous 3D local Nusselt number exhibits significant deviation from the axisymmetric prediction. This difference in local heat transfer can be important when we consider evaporation and combustion of a liquid droplet (or surface reaction of a particle), where the fuel mass fraction on the droplet surface is expressed as an exponential function of droplet surface temperature according to the Clausius-Clapeyron relation. This shows that the mass transfer rate from the droplet is a strong function of local droplet temperature and very sensitive to local heat transfer rate. In such applications, it is important to predict the local behavior of Nusselt number correctly through the 3D calculation.

Acknowledgments

This work was supported by the Center for Simulation of Advance Rockets under a grant from the Department of Energy ASCI program. Prof. Ha wishes to express his appreciation for the financial support provided by LG Yonam Foundation. The computations presented here were performed with computer support from the National Center for Supercomputing Application. PB and SB would like to thank Dr. J. P. Ferry for helping with some of the simulations.

References

- Clift, R., Grace, J. R., and Weber, M. E., 1978, *Bubbles, Drops and Particles*, Academic Press, New York.
- Faeth, G. M., 1983, "Evaporation and Combustion of Sprays," *Prog. Energy Combust. Sci.*, **9**, pp. 1–76.
- Law, C. K., 1982, "Recent Advances in Droplet Vaporization and Combustion," *Prog. Energy Combust. Sci.*, **8**, pp. 171–201.
- Natarajan, R., and Acrivos, A., 1993, "The Instability of the Steady Flow Past Spheres and Disks," *J. Fluid Mech.*, **254**, pp. 323–344.
- Tomboulides, A. G., Orszag, S. A., and Karniadakis, G. E., 1993, "Direct and large-eddy simulation of axisymmetric wakes," *AIAA Paper 93-0546*.
- Johnson, T. A., and Patel, V. C., 1999, "Flow past a sphere up to a Reynolds number of 300," *J. Fluid Mech.*, **378**, pp. 19–70.
- Kurose, R., and Komori, S., 1999, "Drag and lift forces on a rotating sphere in a linear shear flow," *J. Fluid Mech.*, **384**, pp. 183–206.
- Mittal, R., 1999, "A Fourier Chebyshev spectral collocation method for simulation flow past spheres and spheroids," to appear in *Int. J. Numer. Meths. Fluids*.
- Bagchi, P., and Balachandar, S., 2000, "Unsteady motion and forces on a spherical particle in nonuniform flows," *Proceedings of FEDSM 2000*, Boston, MA.
- Sayegh, N. N., and Gauvin, W. H., 1999, "Numerical Analysis of Variable Property Heat Transfer to a Single Sphere in High Temperature Surroundings," *AIChE J.*, **25**, pp. 522–534.
- Ranz, W. E., and Marshall, W. R., 1952, "Evaporation From Drops," *Chem. Eng. Prog.*, **48**, pp. 141–146.
- Whitaker, S., 1972, "Forced Convection Heat Transfer Correlations for Flow in Pipes, Past Flat Plates, Single Spheres, and for Flow in Packed Beds and Tube Bundles," *AIChE J.*, **18**, pp. 361–371.
- Renksizbulut, M., and Yuen, M. C., 1983, "Numerical Study of Droplet Evaporation in a High-Temperature Stream," *ASME J. Heat Transfer*, **105**, pp. 389–397.
- Wong, K., Lee, S., and Chen, C., 1986, "Finite Element Solution of Laminar

- Combined Convection From a Sphere," ASME J. Heat Transfer, **108**, pp. 860–865.
- [15] Yuge, T., 1960, "Experiments on Heat Transfer From Spheres Including Combined Natural and Forced Convection," ASME J. Heat Transfer, **82**, pp. 214–220.
- [16] Chiang, C. H., Raju, M. S., and Sirignano, W. A., 1992, "Numerical Analysis of Convecting, Vaporizing Fuel Droplet With Variable Properties," Int. J. Heat Mass Transf., **35**, No. 5, pp. 1307–1324.
- [17] Xin, J., and Megaridis, C. M., 1996, "Effects of Rotating Gaseous Flows on Transient Droplet Dynamics and Heating," Int. J. Heat Fluid Flow, **17**, pp. 52–62.
- [18] Dandy, D. S., and Dewyer, H. A., 1990, "A Sphere in Shear Flow at Finite Reynolds Number: Effect of Shear on Particle Lift, Drag, and Heat Transfer," J. Fluid Mech., **216**, pp. 381–410.
- [19] Mittal, R., and Balachandar, S., 1996, "Direct numerical simulation of flow past elliptic cylinders," J. Comp. Phys., **124**, pp. 351–367.
- [20] Wu, J.-S., and Faeth, G. M., 1993, "Sphere Wakes in Still Surroundings at Intermediate Reynolds Numbers," AIAA J., **254**, pp. 323–344.
- [21] Mittal, R., and Balachandar, S., 1995, "Effect of three-dimensionality on the lift and drag of nominally two-dimensional cylinders," Phys. Fluids, **7**, pp. 1841–1865.
- [22] Sakamoto, H., and Haniu, H., 1995, "The formation mechanism and shedding frequency of vortices from a sphere in uniform shear flow," J. Fluid Mech., **287**, pp. 151–171.
- [23] Magnaudet, J., Rivero, M., and Fabre, J., 1995, "Accelerated flows past a rigid sphere or a spherical bubble. Part 1. Steady straining flow," J. Fluid Mech., **284**, pp. 97–135.